Electrochimica Acta 301 (2019) 366–376

Contents lists available at ScienceDirect

Electrochimica Acta

journal homepage: www.elsevier.com/locate/electacta

Controlled sulfurization of $MnCO_3$ microcubes architectured MnS_2 nanoparticles with 1.7 fold capacitance increment for high energy density supercapacitor

R.B. Pujari [a, c], V.C. Lokhande [b], U.M. Patil [a], D.W. Lee [c, **], C.D. Lokhande [a, *]

[a] Centre for Interdisciplinary Research, D.Y. Patil Education Society (Deemed to be University), Kolhapur, MS, 416 006, India
[b] Department of Electronics and Computer Engineering, Chonnam National University, 300 Yongbong-Dong, Puk-Gu, Gwangju, 500-757, South Korea
[c] MEMS and Nanotechnology Laboratory, School of Mechanical System Engineering, Chonnam National University, Gwangju, 61186, South Korea

ARTICLE INFO

Article history:
Received 5 November 2018
Received in revised form
17 January 2019
Accepted 18 January 2019
Available online 2 February 2019

Keywords:
$MnCO_3$ microcubes
MnS_2 nanoparticles
Sulfurization
Supercapacitor
Thin film

ABSTRACT

Recently, sulfurization and phosphorylation protocols are employed in porous nano-materials preparation beneficial to improve energy density and power density of pseudocapacitors. Due to well-defined redox activity and higher theoretical capacitance, manganese sulfide electrode is used in supercapacitor application. In present work, $MnCO_3$ microcubes are converted into MnS_2 nanoparticles using cost-effective high diffusion rate sulfurization method. Reducing size of material from microcubes to nanoparticles has facilitated rate capability in the material along with improved capacitance. MnS_2 nanoparticles exhibit 713 Fg^{-1} specific capacitance at 5 mVs^{-1} scan rate compared with 407 Fg^{-1} obtained for $MnCO_3$ microcubes. The impedance study analyzes improvement in interfacial conductivity for MnS_2 nanoparticles observed form 1.83 Ωcm^{-2} equivalent series resistance in comparison with 2.35 cm^{-2} for $MnCO_3$ microcubes.

Fabricated solid state $MnS_2//MoS_2$ asymmetric supercapacitor exhibits 41.7 $Whkg^{-1}$ energy density, and 450 Wkg^{-1} power density with the respectable 88 % capacitance retention for the continuous 2000 CV cycles charging and discharging at 100 mVs^{-1} scan rate.

1. Introduction

Pseudocapacitors are better choice to accomplish high energy density demand without compromising high power density of energy storage devices compared with electrochemical double layer capacitors [1–4]. Owing to low electrical conductivity, transition metal oxide [5–7] based electrodes suffer from low rate capability and low energy density [8–11]. Currently, intensive research is focused on transition metal (TM) chalcogenide based pseudocapacitors for the improvement of rate capability and energy density using various cost-effective chemical methods, such as hydrothermal [12–14], electroless deposition [15–17], electrodeposition [18–20], etc. using 1-dimensional (1-D), 2-dimensional (2-D), and 3-dimensional (3-D) more conductive nanostructures [21]. Such a bottom up cost-effective chemical methods becoming very popular in researchers than expensive top down physical methods. Attempts has been emphasized to making porous and nanostructured materials. Very recently, sulfurization [22–28] and phosphorylation [29–31] treatments of metal oxides are employed to increase porosity and conductivity of electrode materials. In the past decade, different $MnCO_3$ micro/nano structures have been wisely utilised as a template material to prepare hollow and nano structured manganese based sulfide or oxide materials using either acidic etching, high temperature H_2S sulfurization or calcination treatments [32–36].

The present work is intended to obtaining porous and relatively conductive nanostructures of manganese sulfide using sulfurization of $MnCO_3$ microcubes. The sulfurized MnS_2 nanoparticles are obtained at high sulfurization rate and systematically analysed for supercapacitive application in 1 M Na_2SO_4 electrolyte. Moreover, electrochemical charge storage kinetics in $MnCO_3$ and MnS_2 thin films are evaluated using cyclic voltammetry technique. The asymmetric $MnS_2//MoS_2$ supercapacitor is fabricated using MnS_2 and MoS_2 as a positive and a negative window electrodes,

* Corresponding author.
** Corresponding author.
E-mail addresses: mems@jnu.ac.kr (D.W. Lee), l_chandrakant@yahoo.com (C.D. Lokhande).

https://doi.org/10.1016/j.electacta.2019.01.185
0013-4686/

respectively and evaluated for supercapacitive performance.

2. Experimental work

2.1. Synthesis of $MnCO_3$ thin film

$MnCO_3$ thin film was prepared using hydrothermal method at 343 K temperature. All chemicals were purchased from Thomas Baker Pvt Ltd Company. All solutions were prepared in de-ionised water. A 0.1 M 20 ml $MnSO_4$, 0.5 M 20 ml urea (CH_4N_2O) and 0.1 M 10 ml Na_2SO_4 were mixed together in glass beaker under vigorous stirring to form final solution. The final 50 ml solution and well cleaned flexible stainless steel (SS) substrate were transferred to Teflon liner. Teflon liner was sealed in stainless steel autoclave and heated to 373 K temperature for 10 h inside laboratory oven. The autoclave was cooled naturally after hydrothermal treatment. A SS substrate coated with white colour $MnCO_3$ thin film was removed from autoclave, washed repeatedly with de-ionised water and dried in natural light. The weight of $MnCO_3$ coating on SS substrate was 0.7 $mgcm^{-2}$ calculated by weight difference gravimetric method.

2.2. Synthesis of MnS_2 thin film

The as prepared $MnCO_3$ thin film was converted to MnS_2 using solution based sulfurization treatment. In detail, 40 ml 0.5 M Na_2S solution was prepared in de-ionised water and transferred to 60 ml volume Teflon liner autoclave. The $MnCO_3$ thin film was placed inside Na_2S solution. Then, autoclave was sealed and heated to 373 K temperature for 24 h to achieve high diffusion rate sulfurization of $MnCO_3$ thin film. The white colour of $MnCO_3$ thin film was changed to black after sulfurization.

Sulfurization of $MnCO_3$ was similarly performed in identical conditions except changing Na_2S concentrations; such as 0.05 M, and 0.1 M. The sulfurized $MnCO_3$ thin films using 0.05, 0.1, and 0.5 M Na_2S solutions are named as 0.05, 0.1, and MnS_2, respectively in the subsequent part of manuscript. The sulfurized MnS_2 thin film was weighed to be 0.9 $mgcm^{-2}$. Sulfurization treatment of $MnCO_3$ thin film was also carried at room temperature (300 K) using various concentrations (0.05, 0.1 and 0.5 M) of Na_2S solutions (Explained in supplementary information).

2.3. Characterization of thin films

All $MnCO_3$ and sulfurized thin films were structurally analysed by X-ray diffraction technique using Bruker D2 phase X-ray diffractometer. Elemental valence states of MnS_2 thin film was studied using X-ray photo emission spectroscopy (XPS) technique. Surface morphology of $MnCO_3$ and sulfurized thin films was visualised via field-emission scanning electron microscopy (FE-SEM). Particle size confirmation and structural analysis of MnS_2 nanomaterial were analysed from transmission electron microscopy (TEM). Surface area of MnS_2 and $MnCO_3$ materials was assessed by Brunauer-Emmett-Teller (BET) surface area analysis using a BET, Micromeritics (ASAP2010) model. Supercapacitive analyses of thin films were carried by cyclic voltammetry, and galvanostatic charge-discharge measurements using aqueous 1 M Na_2SO_4 electrolyte. The impedance spectroscopy study of $MnCO_3$ and sulfurized thin films was performed within frequency range of 0.1–100 kHz at 10 mV ac amplitude.

2.4. Fabrication of MnS_2//MoS_2 asymmetric supercapacitor

For the fabrication of MnS_2//MoS_2 asymmetric supercapacitor, large area (5×5 cm^2) MoS_2 thin film was prepared using chemical bath deposition method explained in the supplementary information. Also, large area (5×5 cm^2) flexible MnS_2 thin film was prepared by hydrothermal treatment of $MnCO_3$ thin film in 0.5 M Na_2S solution for 373 K temperature. Solid-state supercapacitor design was achieved using PVA:Na_2SO_4 hydrogel prepared with the ratio of 1:1. The PVA:Na_2SO_4 hydrogel was painted over a large area (5×5 cm^2) MnS_2 and MoS_2 thin films with subsequent overnight drying. After hydrogel drying, electrodes were prepared by cutting hydrogel painted MnS_2 and MoS_2 thin films. Then, electrodes were sealed at the edges to eliminate direct contact of electrodes during fabrication process of MnS_2//MoS_2 asymmetric supercapacitor.

3. Results and discussion

3.1. Structural and surface morphological analyses

In solution based thin film synthesis methods, very thin (in several nanometres to few micrometre thickness) layer of material is prepared on the substrate using controlled precipitation strategy. For present work, $MnCO_3$ thin film was formed on SS substrate using urea as hydrolysing agent given by following equation.

$$3MnSO_4 + 5CON_2H_4 + 6H_2O \rightarrow 3MnCO_3 + 10NH_3 + 2CHO + 3SO_4 \quad (1)$$

Then, $MnCO_3$ thin film is converted into MnS_2 thin film at 373 K temperature by high rate sulfurization treatment shown in Fig. 1. Sodium sulfide produces hydrogen sulfide (H_2S) by dissolving in H_2O as shown in following equation.

$$Na_2S + 2H_2O \rightarrow H_2S + 2NaOH \quad (2)$$

In present work, second hydrothermal treatment (Fig. 1) expose high diffusion process of H_2S vapours in $MnCO_3$ thin film. Hydrogen sulfide molecules diffuse into $MnCO_3$ microcubes and using long exposure (24 h) of H_2S vapours, microcubes surface of $MnCO_3$ is converted into porous and nano structured. As shown in Fig. 1, H_2S diffusion rate is highly enhanced by increasing Na_2S concentration from 0.05 M to 0.5 M to reduce size of material from micrometre to nanometre range with increasing porosity. Thus, increasing H_2S diffusion rate, surface morphology has been changed from microcubes to nanodiscs, nanosheets, and nanoparticles shown by schematic Fig. 1. At very high diffusion rate of H_2S in 0.5 M Na_2S solution, $MnCO_3$ microcubes are converted to MnS_2 nanoparticles indicated with following equation.

$$MnCO_3 + 2H_2S \rightarrow MnS_2 + 2H_2O + 2CO \quad (3)$$

MnS_2 phase of manganese sulfide was also obtained by Yu et al. [37] using S:Mn precursors ratio higher than 4:1 on tin doped indium oxide (ITO) substrate. Sulfurizing of metal oxide or carbonate precursors using H_2S gas is already performed in the literature. Liu et al. [22] reported synthesis of NiO thin film and sulfurization treatment converted to NiO@Ni_3S_4 thin films at low (0.05 M) Na_2S concentration for different sulfurization times [22]. In another work, $MnCO_3$ microboxes are converted into MnS microboxes at very high temperature of 1073 K by H_2S sulfurization using chemical vapour deposition method [23].

The X-ray diffraction pattern of $MnCO_3$ thin film shows the (012), (104), (110), (113), (202), (108) peaks well matches with the JCPDS card no. 44-1472 that dictates formation of rhombohedral crystal structure of $MnCO_3$ (Fig. 2 (A)). The Δ peaks observed in $MnCO_3$ sample correspond to SS substrate. For XRD analysis of sulfurized samples at 0.1 and 0.5 Na_2S concentrations, peeled off powder samples (Thin films are peeled off from stainless steel substrate) are used due to low crystalline property of material.

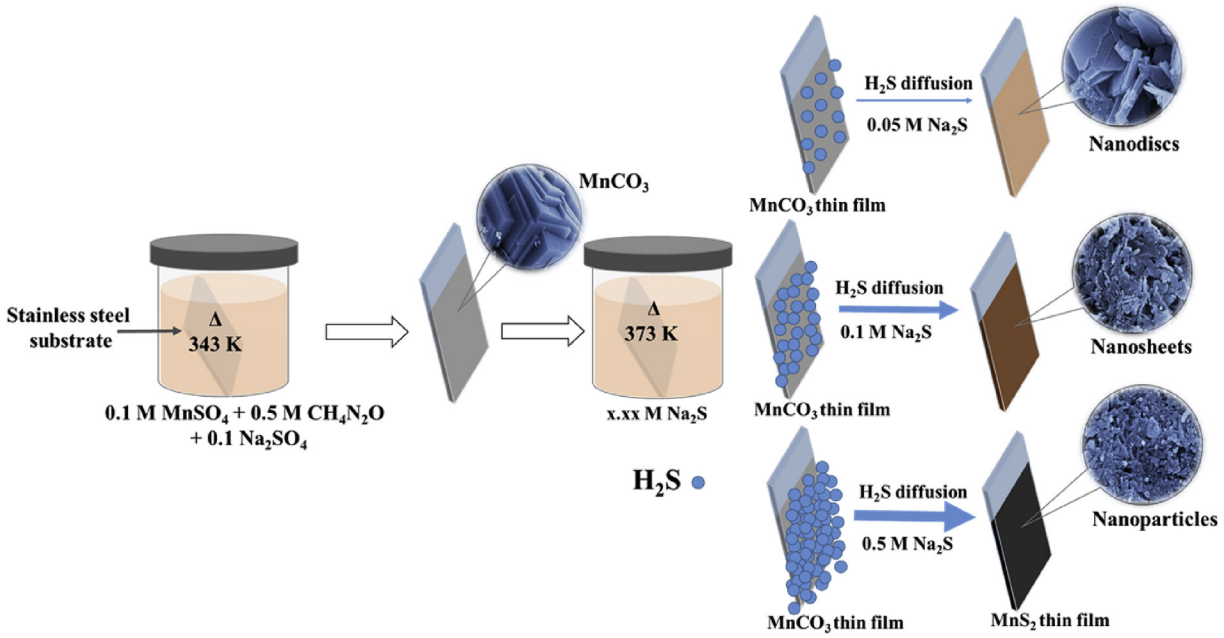

Fig. 1. A schematic for controlled sulfurization of $MnCO_3$ thin film for conversion into nanostructured thin films with the morphological hierarchy.

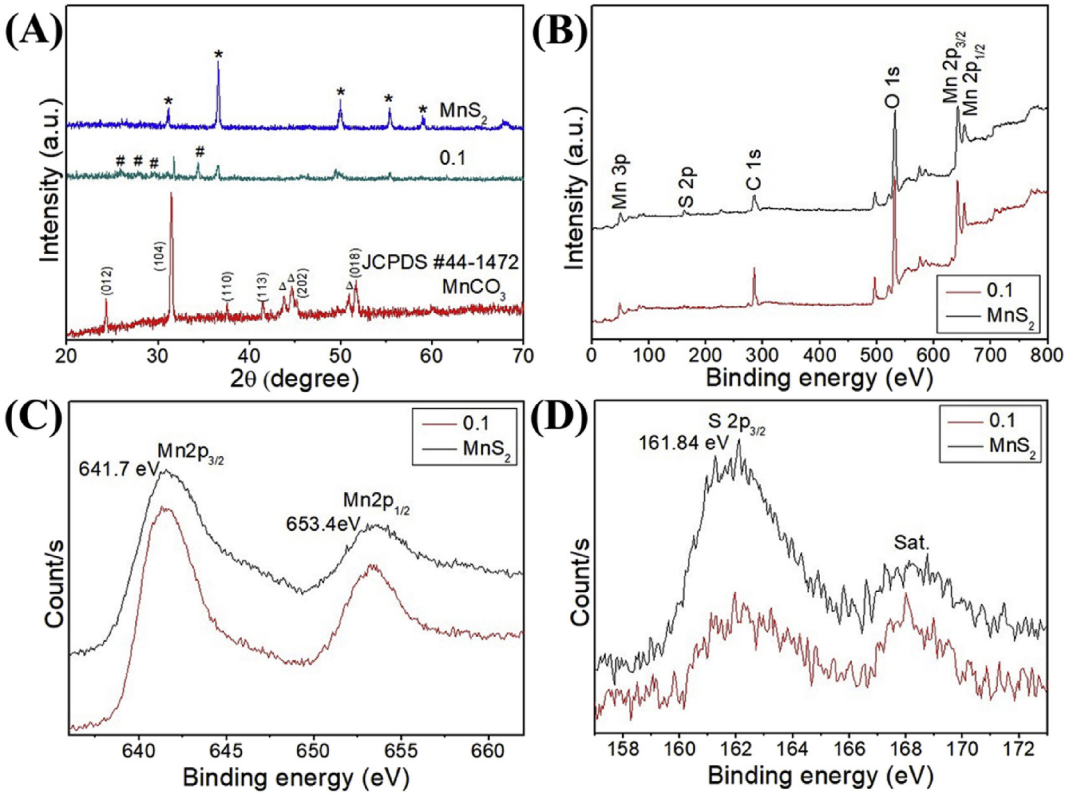

Fig. 2. (A) X-ray diffraction patterns of $MnCO_3$ and sulfurized thin films, and comparative XPS spectra for (B) survey scan, (C) Mn 2p, and (D) S 2p of 0.1 and MnS_2 thin films.

Sulfurized thin film at 0.1 M Na_2S concentration show presence of MnS and MnS_2 phases of manganese sulfide. For higher sulfurization rate (0.5 sample), $MnCO_3$ is completely converted to MnS_2 phase. Survey scan XPS spectra (Fig. 2 (B)) of mixed phase manganese sulfide and MnS_2 thin films show presence of manganese, and sulphur elements in the material. XPS peaks at 641.7 and 653.4 eV binding energies correspond to $Mn2p_{3/2}$ and $Mn2p_{1/2}$ energies of manganese indicating +4 valence state (Fig. 2 (C)) of manganese. Further, energy gap of 11.7 eV between $Mn2p_{3/2}$ and $Mn2p_{1/2}$ states of manganese confirms Mn^{+4} state consistent with literature. XPS spectra of sulphur is observed for $S2p_{3/2}$ energy state at binding energy of 161.84 eV that confirms formation of MnS_2, while satellite peak at higher binding energy of 168.2 eV suggest air oxidation of sample (Fig. 2 (D)).

Surface morphology of $MnCO_3$ and sulfurized thin films (Fig. 3) show micro and nanostructure surface, respectively. Very fine and smooth surface interlocked microcubes are seen for $MnCO_3$ thin film as in Fig. 3(A) and (B). The microcubes surface of $MnCO_3$ is broken down to porous and nanostructured, comprising nanodiscs with average thickness of 5–100 nm at 0.05 M Na_2S sulfurization seen from Fig. 3(C) and (D). For 0.1 sample, micro-surface of $MnCO_3$ is changed to porous nanostructure with encompassing nanosheets and nanoparticles (Fig. 3(E) and (F)). At very high sulfurization rate (i.e. at 0.5 M Na_2S) $MnCO_3$ surface microstructure has been converted to MnS_2 nanoparticles (Fig. 3(G) and (H)). MnS_2 thin film formed with very fine nanoparticles of the size ranging with 10–20 nm. The nanoparticles are randomly distributed on film surface with comprising pores of 5–100 nm in size. Thus, simple solution based chemical protocol has been converted from microstructure of $MnCO_3$ thin film to nanostructured MnS_2 thin film. For room temperature (300 K) sulfurization of $MnCO_3$ thin films, sulfurized thin films exhibit comparatively less porous surface morphology as observed in Fig. S1.

Fig. 4 (A) shows TEM image of MnS_2 comprising very fine nanoparticles ranging with 10–15 nm sizes consistent with FE-EM images of MnS_2 sample. High-resolution TEM images in Fig. 4 (B), and (C) show arrangement of MnS_2 crystal lattices with the interplanar spacing 0.286 and 0.239 nm consistent with the XRD

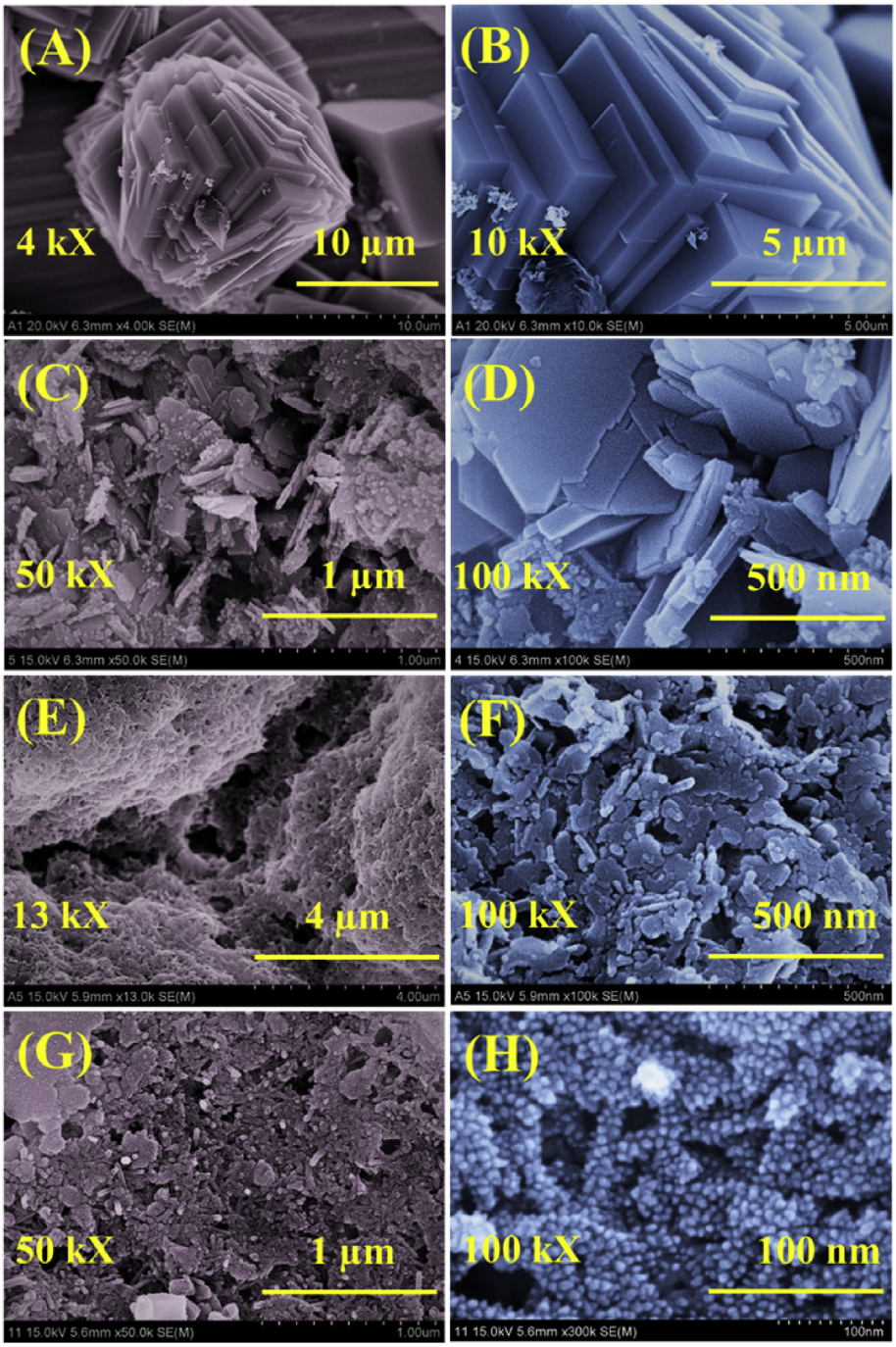

Fig. 3. Field-emission scanning electron microscopy (FE-SEM) images of (A), and (B) $MnCO_3$ thin film. The other FE-SEM images for sulfurization treatment of $MnCO_3$ with varying Na_2S concentration; (C) and (D) for 0.05 M, (E) and (F) for 0.1 M, and (G), (H) for 0.5 M.

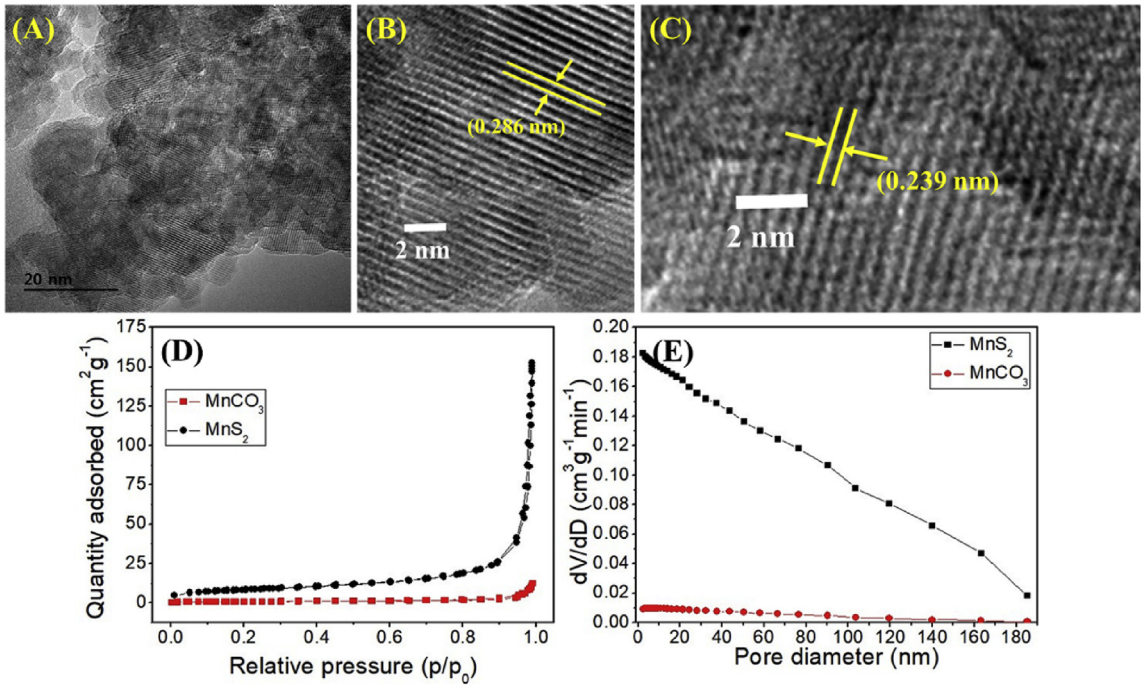

Fig. 4. (A) Transmission electron microscopy (TEM) image of MnS_2 nanoparticles at 20 nm resolution, (B), and (C) high-resolution TEM images showing inter-planar spacing of 0.286 and 0.239 nm for lattice arrangement of MnS_2 material, (D) comparative N_2 adsorption-desorption curves of MnS_2, and $MnCO_3$ samples, and (E) pore size distribution, respectively.

analyses of material. Specific surface area of MnS_2, and $MnCO_3$ materials is obtained using N_2-adsorption desorption isotherms presented in Fig. 4 (D) that indicates presence of higher surface area for MnS_2. The highest surface area of 56.5 m^2g^{-1} is obtained for MnS_2 using Brunaeur-Emmett-Teller surface area analysis comparison with 2 m^2g^{-1} for $MnCO_3$ microcubes. Pore size distribution of MnS_2, and $MnCO_3$ is fitted using Barrett-Joyner-Halenda (BJH) model (Fig. 4 (E)), showing typical adsorption macroporous solids with weak adsorption present in the MnS_2 material useful for advanced electrochemical applications, such as supercapacitor, gas sensor, electrocatalysts etc.

3.2. Supercapacitive properties

Supercapacitive charge storage in $MnCO_3$ and all sulfurized MnS_2 thin films is evaluated using 1 M Na_2SO_4 electrolyte by cyclic voltammetry (CV) and galvanostatic charge-discharge (GCD) techniques. $MnCO_3$ and other sulfurized thin films are employed to CV measurements recorded at 20 mVs^{-1} scan rate within operating potential window of 0 to +1.1 V/SCE seen in Fig. 5 (A). The charge storage in $MnCO_3$ and sulfurized thin films is proposed by following equations,

$$MnCO_3 + Na^+ + e^- \leftrightarrow MnCO_3Na \quad (4)$$

$$MnS_x + Na^+ + e^- \leftrightarrow MnS_xNa \quad (5)$$

Comparative CV curves show highest recorded area under CV curve for MnS_2 thin film than other thin films. All CV curves of room temperature sulfurized $MnCO_3$ thin films also recorded at different scan rates shown in Fig. S2, which have less integrated CV area than MnS_2 thin film. Fig. 5 (A) shows decreasing trend of redox peak intensities with increasing sulfurization treatment of $MnCO_3$ thin film attributed to nanostructured material for higher sulfurized thin films. To obtain rate capability and capacitance of both $MnCO_3$ and MnS_2 thin films, different scan rates of CV curves are recorded from 100 to 5 mVs^{-1} as in Fig. 5(B) and (C). All CV curves for MnS_2 thin films show approximate rectangular shape, signify more capacitive charge storage feature compared to $MnCO_3$. For both $MnCO_3$ and MnS_2 thin films, increasing scan rates of CV curves shifted oxidation peak in positive direction, while reduction peak in negative direction and small difference between reduction and oxidation peaks dictates presence of more reversible redox charge storage. CV curves of $MnCO_3$ thin film show redox peaks that are relatively deeper than MnS_2 for each scan rates, indicate presence of more diffusion controlled character in $MnCO_3$.

More insights are provided using cyclic voltammetry analyses on the charge storage mechanism of both thin films. Fig. 5 (D) dictates log (current density) versus log (scan rate) plots for $MnCO_3$ and MnS_2 thin films obtained from CV curves as follows,

$$i = av^b \quad (6)$$

where, a and b can be adjusted; with b as a slope of curve in Fig. 5 (D). For the linear relation between current and sweep rate, b becomes to 1 and corresponding charge storage is defined to be capacitive, whereas for semi-infinite diffusion induced charge storage, b value becomes 0.5. For the $MnCO_3$ and MnS_2 thin films, current densities at 0.4 V/SCE potential shows slope values of 0.55 and 0.82, respectively. Thus, charge storage mechanism in $MnCO_3$ and MnS_2 thin films mainly based upon diffusion controlled (Q_D) and surface capacitive (Q_S), respectively. However, for each current density of CV curve, charge storage mechanism can be divided into both diffusion controlled and surface capacitive for semi-infinite diffusion, calculated with the following relation.

$$Q = Q_S + Q_D \quad (7)$$

Here, Q_S is combination of surface electron transfer reactions induced charges and electrostatically generated charges due to double layer formation, while Q_D is existed by Na^+ ion diffusion process into bulk electrode. For the semi-infinite linear diffusion, total charges stored in the material can be expressed with following equation.

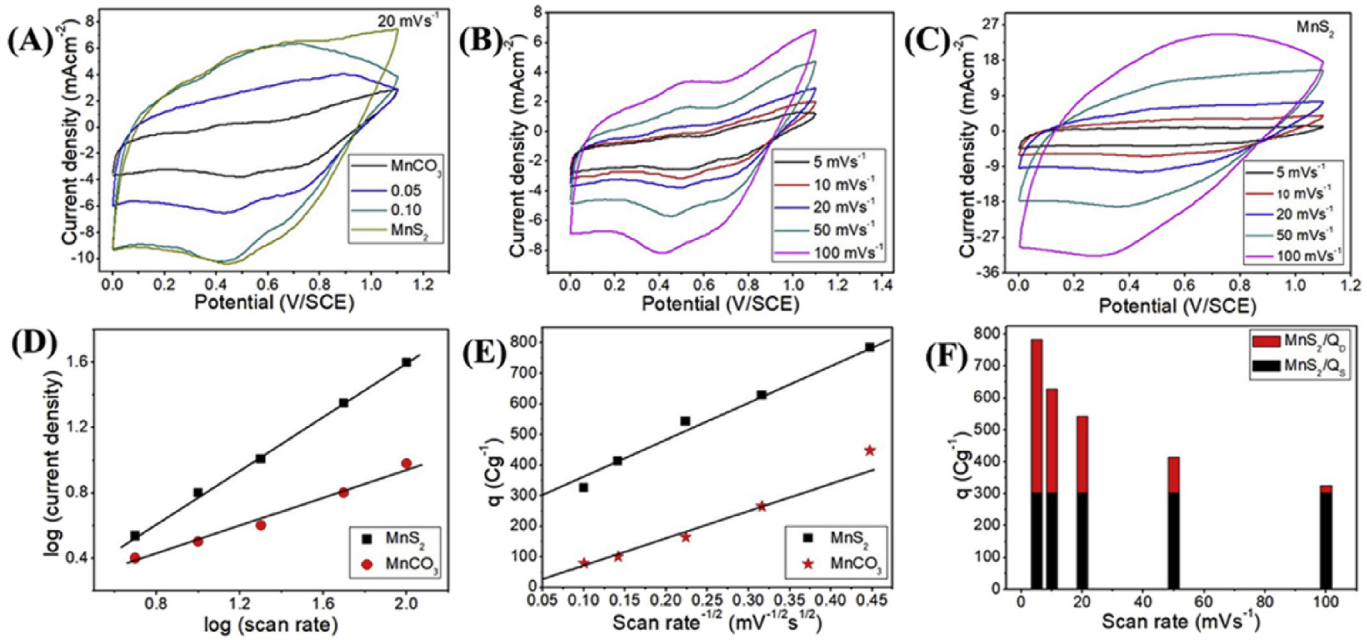

Fig. 5. (A) Cyclic voltammetry (CV) charging and discharging curves at 20 mVs^{-1} scan rate of different manganese based thin film samples measured in 1 M Na_2SO_4 electrolyte, (B) and (C) CV curves of $MnCO_3$ and MnS_2 thin films, respectively ranging with 5–100 mVs^{-1} scan rates, (D) the log (current density) versus log (scan rate) plot of anodic current response at 0.4 V/SCE potential, (E) linear relation between charge storage (q) of MnS_2 and $MnCO_3$ thin films versus scan $rate^{-1/2}$ and (F) distribution of capacitive and diffusion controlled charge storage in MnS_2 thin film with changing scan rate of CV curves.

$$Q = Q_S + cv^{-0.5} \tag{8}$$

where, c is constant and v is scan rate of CV curve. However, this relation cannot best fitted for high scan rate of CV curves due to polarization effect of the charges. Fig. 5 (E) shows linear relation of total Q charges stored in the material with the product of $cv^{-0.5}$ obtained for each scan rates. The Q versus $cv^{-0.5}$ line intersection to Q axis gives surface capacitive charge storage (Q_S) of the material. For MnS_2 thin film, Q_S value of 302 Cg^{-1} is much higher than 24 Cg^{-1} obtained for $MnCO_3$. Using Q_S value of MnS_2 thin film, contribution of capacitive and diffusion controlled charge storage is calculated at each scan rate shown in Fig. 5 (F), which is highest (92.75 %) for 100 mVs^{-1} and decreases to 38.5 % at the low scan rate of 5 mVs^{-1}.

However, for the $MnCO_3$ case, capacitive storage becomes 35.54 % at 100 mVs^{-1} scan rate, which reduces to 5.35 % at the scan rate of 5 mVs^{-1} seen in Fig S3 (A). Thus, it is concluded that charge storage mechanism of $MnCO_3$ thin film near to cathodic peak is more likely to be diffusion controlled, while it is likely to be capacitive for MnS_2 case. Comparative column paper data presented in Fig. S3 (B) shows percentage capacitive charge storage at different scan rates for MnS_2 and $MnCO_3$ thin film with varying scan rates. It dictates that charges stored in the MnS_2 thin film at higher scan rate of 100 mVs^{-1} are highly dominated ($Q_S = 93$ %) by surface capacitive mechanism, while for the $MnCO_3$ thin film, at higher scan rate, charge storage is still dominated ($Q_S = 31$%) by diffusion controlled mechanism. It is due to more conducting and nanostructured surface of MnS_2 thin film.

The specific capacitance of MnS_2 and $MnCO_3$ thin films is compared in Fig. 6 (A), calculated at various scan rates using following relation,

$$C_S = \frac{1}{mv}\int_{V1}^{V2} I\Delta V dt \tag{9}$$

where, C_S is specific capacitance, m is deposited weight of thin film on SS substrate, v is scan rate of CV curve, I is current density as function of applied potential, and ΔV is operating potential window of thin film. The highest 713 Fg^{-1} capacitance of MnS_2 is achieved at 5 mVs^{-1} scan rate and retained to 297 Fg^{-1} with increasing scan rate to 100 mVs^{-1}. For $MnCO_3$ thin film, capacitance of 407 Fg^{-1} is observed at 5 mVs^{-1} and reduced to 71.5 Fg^{-1} at 100 mVs^{-1}. The obtained highest capacitance for MnS_2 nanoparticles in present work is greater than the capacitances obtained for the MnS microfiber (538.5 Fg^{-1}) [38], MnS nanoparticles (710.6 Fg^{-1}) [39], manganese sulfide nanocrystals (704.5 Fg^{-1}) [40], MnS/GO-NH_3 nanoparticles (390.8 Fg^{-1}) [41], α-MnO_2 nanowires (310.2 Fg^{-1}) [42], and β-MnO_2/Birnessite (657.2 Fg^{-1}) [43] shown in Table 2. As obtained highest capacitance of MnS_2 thin film in present work is attributed to 1 dimensional nanoparticles surface nanostructure of conducting MnS_2 than its oxide counterpart.

The galvanostatic charge-discharge (GCD) measurements of $MnCO_3$ and all sulfurized thin films are performed at 1 $mAcm^{-2}$ current density compared in Fig. 6 (B). It shows highest discharging time for MnS_2 thin film attributed to maximum reversible redox reactions between Na^+ and MnS_2 nanoparticles. Moreover, initial voltage drop is less for MnS_2 thin film due to more conductive feature of fully sulfurized MnS_2 thin film observed in impedance analyses presented later in this section. The GCD measurements of MnS_2 and $MnCO_3$ thin films also performed at different applied current densities varied from 1 to 16 $mAcm^{-2}$ shown in Fig. 6(C) and (D), respectively. All GCD curves of $MnCO_3$ show initial IR voltage drop more in magnitude than corresponding GCD curves for MnS_2 thin film. Both thin films show non-linear discharge curves for all current densities suggesting pseudocapacitive feature. The specific capacitances of both the thin films are calculated from GCD profiles for various current densities shown in Fig. 7 (A) using following relation,

$$C_S = \frac{It_d}{m\Delta V} \tag{10}$$

where, t_d (s) is discharging time of thin film for applied constant

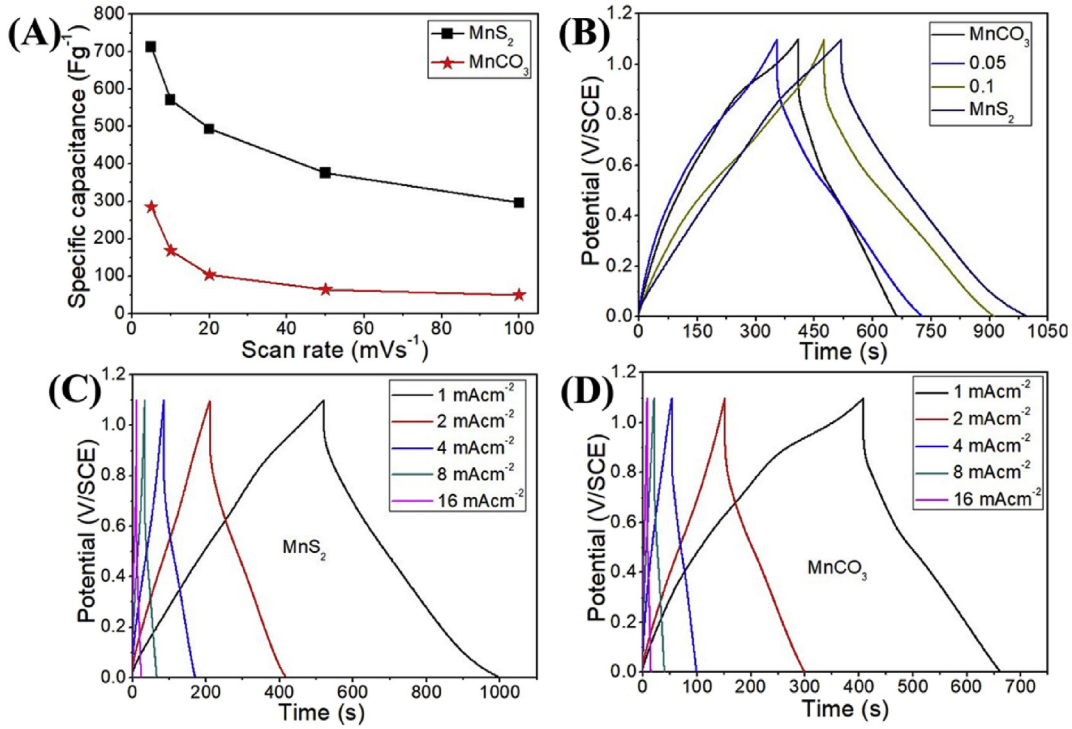

Fig. 6. (A) Comparison of specific capacitance of $MnCO_3$ and MnS_2 thin films with increasing scan rates from 5 to 100 mVs^{-1}, (B) galvanostatic charge-discharge (GCD) of manganese based thin films including $MnCO_3$ and all sulfurized thin films, (C) and (D) GCD curves of MnS_2 and $MnCO_3$ thin films, respectively with changing current density from 1 to 16 $mAcm^{-2}$.

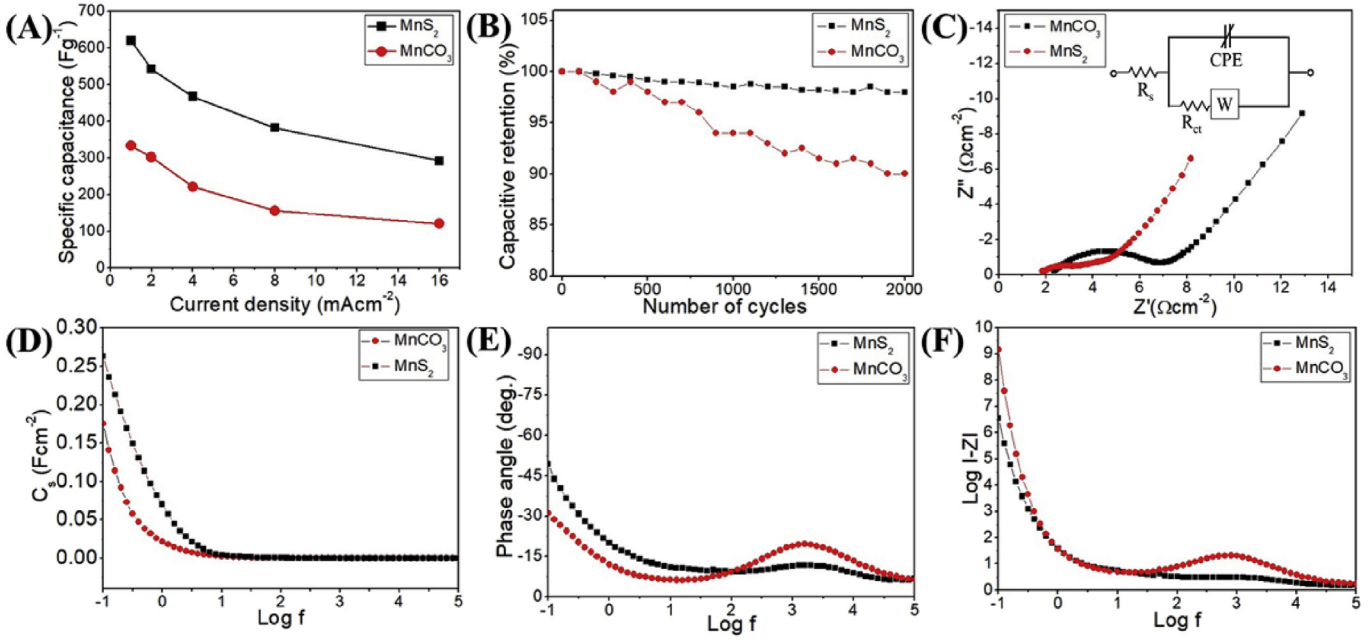

Fig. 7. (A) Current density dependant specific capacitance of $MnCO_3$ and MnS_2 thin films, (B) capacitive retention of thin films for continuous 2000 CV cycles measured at 100 mVs^{-1} scan rate, (C) Nyquist plots of $MnCO_3$ and MnS_2 thin films measured in frequency range of 0.1–10^5 Hz at 10 mV ac amplitude, with inset showing best fitted equivalent circuit, and frequency dependant variation of (D) areal capacitance, (E) Bode plot, and (F) magnitude of imaginary part of impedance of MnS_2 and $MnCO_3$ thin films.

current density I ($mAcm^{-2}$). The maximum capacitance of 620 Fg^{-1} is achieved for MnS_2 thin film, which is more than 343 Fg^{-1} obtained for $MnCO_3$ thin film at the same current density of 1 $mAcm^{-2}$ shown in Fig. 7 (A). The increased capacitance in the MnS_2 thin film is result of highly conducting and maximum electroactive nanostructured surface of MnS_2. Lifetime of both thin films is evaluated for continuous 2000 CV cycles recorded at 100 mVs^{-1} scan rate shown in Fig. 7 (B). The 98% capacitance is remained for MnS_2 thin film after continuous cycling, which is higher than 90% observed for $MnCO_3$ thin film. It is due to higher conductive MnS_2

nanostructure surface and contribution of capacitive charge storage reactions for MnS_2 thin film that sustains material reversibility for large number of charge-discharge cycling process.

Electrochemical impedance spectroscopy technique is employed to analyse different frequency dependant impedance features of MnS_2 and $MnCO_3$ thin films in 1 M Na_2SO_4 electrolyte. The comparative Nyquist plots of both thin films (Fig. 7 (C)) gives equivalent series resistance (R_s) in high frequency region, charge transfer resistance (R_{ct}) in mid frequency region, and Warburg resistance (W) in low frequency region. Inset of Fig. 7 (C) presented corresponding equivalent circuit model best fitted for Nyquist plots for MnS_2 and $MnCO_3$ thin films. The reduction of R_s (1.83 Ωcm^{-2}) and R_{ct} (1.49 Ωcm^{-2}) values for MnS_2 thin film attributed to more conducting and nanostructured material formation of MnS_2 thin film. For $MnCO_3$ thin film, these values are obtained as 2.35 Ωcm^{-2} and 4.51 Ωcm^{-2}, respectively (Table (1)). Frequency dependant areal capacitance, Bode plot, and log (mod (-z)) Impedance plot are presented in Fig. 7(D–F), respectively. Frequency dependant capacitance study demonstrates better charge storage kinetics behaviour of MnS_2 compared to $MnCO_3$ in the middle and lower frequency region. Diffusion controlled behaviour in the middle frequency region of both thin films is reflected from Bode plot and log (mod (-z)) plot. Further, Bode plot suggests better super-capacitive feature of MnS_2 thin film.

4. MnS_2//MoS_2 asymmetric supercapacitor

For the fabrication of MnS_2//MoS_2 supercapacitor, large area MnS_2 and MoS_2 thin films were prepared. Nano-grain composed surface morphology of MoS_2 thin film is observed from FE-SEM images in Fig. S4 (A) and (B). The CV curves of MoS_2 thin film are obtained from 5 to 100 mVs^{-1} scan rates within negative potential window of −1.2 to 0 V/SCE in 1 M Na_2SO_4 electrolyte to analyse capacitance and rate capability (Fig. S5 (A)). Further, non-linear GCD curves of MoS_2 thin film are presented in Fig. S5 (B). The maximum 337 and 291 Fg^{-1} specific capacitances of MoS_2 thin film are obtained using equations (6) and (7) from CV and GCD curves (Fig. S5 (C and D)) at 5 mVs^{-1} and 1 $mAcm^{-2}$, respectively. The cycling stability of MoS_2 thin film is performed for continuous 2000 CV cycles scanned at 100 mVs^{-1} scan rate. The capacitive retention of 88 % is achieved for MoS_2 thin film in 1 M Na_2SO_4 electrolyte (Fig. S6 (A)). For the MoS_2 thin film, shape of CV curve is not much influenced after cycling (inset of Fig. S6 (B)), attributed to good reversibility of material in Na_2SO_4. Further, impedance spectrum of MoS_2 thin film shows 0.46 and ~4 Ωcm^{-2} series and charge transfer resistances shown in Fig. S6 (C).

Fabricated MnS_2//MoS_2 supercapacitor is evaluated for charge storage using CV and GCD techniques with MnS_2 and MoS_2 thin films are cathode and anodes, respectively shown in Fig. 8 (A–C). To obtain maximum capacitance of supercapacitor, weight of MnS_2

Table 1
Improvement in specific capacitance and ESR values of manganese based thin films using high diffusion rate sulfurization.

Sr. no.	Name of material	Surface microstructure	Surface charge storage at 100 mVs^{-1} (Q_S) (Cg^{-1})	Diffusion controlled charge storage at 100 mVs^{-1} (Q_D) (Cg^{-1})	Total charge storage at 5 mVs^{-1} (Q_S) (Cg^{-1})	Specific capacitance (Fg^{-1})	ESR (Ωcm^{-2})
1	MnS_2	Nanoparticles	302 (92.75%)	23.6 (7.25%)	784	713	1.83
2	$MnCO_3$	Microcubes	24 (30.54%)	54.57 (69.46%)	447	407	2.35

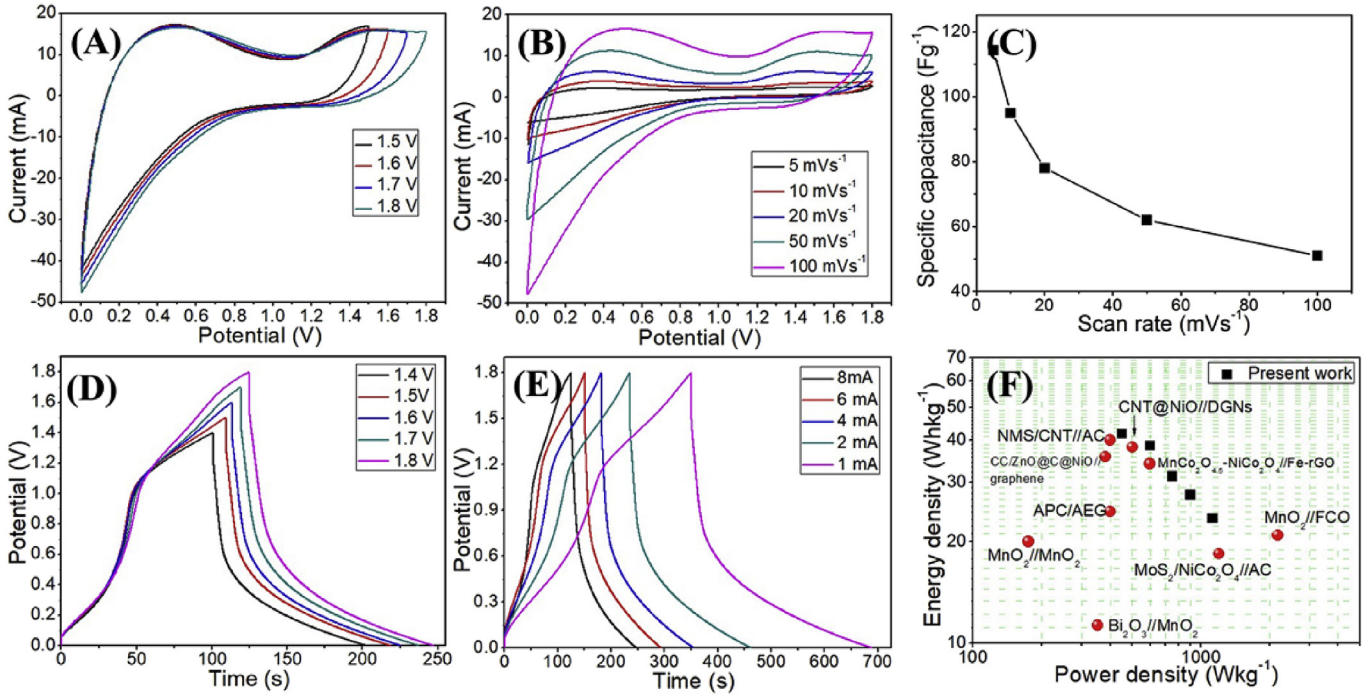

Fig. 8. (A) CV curves of fabricated MnS_2//MoS_2 supercapacitor with different potential window ranging from 1.5 to 1.8 V, (B) CV curves of device with different scan rates, (C) variation in specific capacitance of device with the scan rate, (D) charging and discharging measurement of device at 6 mA applied current for various potential windows, (E) GCD curves of supercapacitor at 1.8 V potential window with increasing current, ranging from 6 to 15 mA, and (F) Ragone plot of MnS_2//MoS_2 asymmetric supercapacitor.

and MoS_2 thin films are balanced using equation S1. The highest capacitance of 114 Fg^{-1} is calculated at 5 mVs^{-1} scan rate for the potential window of 1.8 V shown in Fig. 8 (C). The better capacitance value of $MnS_2//MoS_2$ supercapacitor is attributed to nanostructure cathode (MnS_2) and anode (MoS_2) surfaces useful for higher reversible redox activity of material. Capacitance is still remained to 51 Fg^{-1} at the highest scan rate of 100 mVs^{-1}, showing good rate capability of supercapacitor. The GCD technique is employed to determine energy and power densities of asymmetric supercapacitor (Fig. 8 (D–F)). An operating potential window (1.4–1.8 V) and applied current (1–6 mA) of supercapacitor are varied to analyse rate capability. The highest energy density of 41.7 $Whkg^{-1}$ is obtained for $MnS_2//MoS_2$ supercapacitor at the power delivery of 450 Wkg^{-1} calculated using equations (S2) and (S3).

The obtained energy and power densities of device are comparable with the earlier report in the literature such as 11.3 $Whkg^{-1}$ and 352.6 Wkg^{-1} for $Bi_2O_3//MnO_2$ [44], 20 $Whkg^{-1}$, and 175 Wkg^{-1} for $MnO_2//MnO_2$ [45], 24.6 $Whkg^{-1}$, and 400 Wkg^{-1} for APC/AEG [46], 40 $Whkg^{-1}$, 400 Wkg^{-1} for NMS/CNT//AC [47], 18.4 $Whkg^{-1}$, and 1200.2 Wkg^{-1} for $MoS_2/NiCo_2O_4//AC$ [48], 35.7 $Whkg^{-1}$, and 380.9 Wkg^{-1} for CC/ZnO@C@NiO//graphene [49], 20.9 $Whkg^{-1}$, and 2173.9 Wkg^{-1} for MnO_2//FCO [50], 38.1 $Whkg^{-1}$, and 500 Wkg^{-1} for CNT@NiO//DGNs [51], and 34 $Whkg^{-1}$, and 597.18 Wkg^{-1} for $MnCo_2O_{4.5}$-$NiCo_2O_4$//Fe-rGO [52] supercapacitors, respectively (Table 3). Lifetime of $MnS_2//MoS_2$ supercapacitor is evaluated by continuous charging and discharging for 2000 CV cycles measured at 100 mVs^{-1} scan rate. A 88% capacitance retention is observed for supercapacitor after CV cycling shown in Fig. 9 (A). Small change in CV curve is dictated inset of Fig. 9 (A).

The impedance spectrum of $MnS_2//MoS_2$ supercapacitor is obtained within frequency range of 0.1–100 kHz for AC amplitude of 10 mV presented in Fig. 9 (B). Low ESR (0.6 Ω) and R_{ct} (4.6 Ω) values

Table 2
Comparison of capacitances of materials prepared by different methods in literature with present work MnS_2 material.

Sr. no.	Name of material	Method of preparation	Electrolyte	Potential window (V)	Specific capacitance (Fg^{-1})	Ref
1	MnS microfibers	Chemical bath deposition	1 M KOH	1.2	538.5 (5 mVs^{-1})	[38]
2	MnS nanoparticles	Hydrothermal	1 M LiCl	0.8	710.6 (5 mVs^{-1})	[39]
3	manganese sulfide nanocrystals	Hydrothermal	1 M KOH	0.7	704.5 (1 mVs^{-1})	[40]
4	MnS/GO-NH_3 Nanoparticles	Solvothermal	2 M KOH	0.7	390.8 (0.25 Ag^{-1})	[41]
5	α-MnO_2 nanowires @ ultrathin δ-MnO_2	Hydrothermal	6 M KOH	0.65	310.2 (0.5 Ag^{-1})	[42]
6	β-MnO_2/Birnessite	Electrodeposition and hydrothermal	1 M Na_2SO_4	1.0	657.2 (0.25 Ag^{-1})	[43]
7	MnS_2 nanoparticles	Hydrothermal	1 M Na_2SO_4	1.1	713 (5 mVs^{-1})	Present work

Table 3
Different specifications of supercapacitors fabricated using different electrode materials compared with present work $MnS_2//MoS_2$ supercapacitor.

Sr. no.	Asymmetric supercapacitor	Potential window (V)	Specific capacitance (Fg^{-1})	Specific energy ($Whkg^{-1}$)	Specific power (Wkg^{-1})	Cycle life	Ref
1	$Bi_2O_3//MnO_2$	1.8	25.2	11.3	352.6	–	[44]
2	$MnO_2//MnO_2$	1.4	–	20	175	–	[45]
3	APC/AEG	1.6	69	24.6	400	–	[46]
4	NMS/CNT//AC	1.6	108	40	400	100% (10000 cycles)	[47]
5	$MoS_2/NiCo_2O_4//AC$	1.6	51.7	18.4	1200.2	98.2 (2000 cycles)	[48]
6	CC/ZnO@C@NiO//graphene	1.5	–	35.7	380.9	(87.5% (10000 cycles)	[49]
7	MnO_2//FCO	2.0	117	20.9	2173.9	90% (2000 cycles)	[50]
8	CNT@NiO//DGNs	1.6	108	38.1	500	94% (10000 cycles)	[51]
9	$MnCo_2O_{4.5}$-$NiCo_2O_4$//Fe-rGO	1.2	170.8	34	597.18	90% (3000 cycles)	[52]
10	$MnS_2//MoS_2$	1.8	92	41.7	450	88% (2000 cycles)	Present work

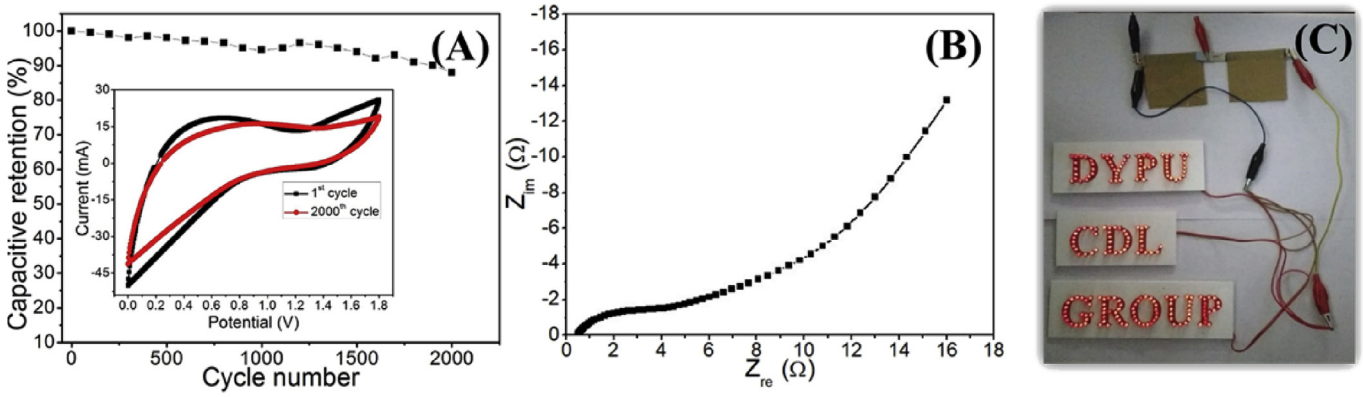

Fig. 9. (A) Capacitive retention of supercapacitor with the increasing charging and discharging CV cycles measured at 100 mVs^{-1}, inset shows CV curves before and after cycling of supercapacitor, (B) impedance spectrum of device in the frequency range of 0.1–10^5 Hz, and (C) practical charge storage demonstration of asymmetric $MnS_2//MoS_2$ supercapacitor for lit up 205 light emitting diodes using series combination of two devices.

are consistent with high energy and power density values of supercapacitor. Practical demonstration of supercapacitor is exhibited from Fig. 9 (C). It shows discharging of two series fashion connected MnS_2//MoS_2 supercapacitors to produce intense glow of 205 red light emitting diodes connected in parallel.

5. Conclusions

MnS_2 nanoparticles are successfully prepared from $MnCO_3$ precursor using cost-effective high sulfurization rate. Increasing sulfurization rate of $MnCO_3$ microcubes has obtained hierarchical surface morphology as nanodiscs, nannosheets and nanoparticles. The electrochemical charge storage analyses of nanostructured MnS_2 thin film has presented charge storage kinetics favourable to capacitive type in comparison with diffusion controlled behaviour for $MnCO_3$ microstructure. The highest 713 Fg^{-1} capacitance is achieved for MnS_2 thin film at 5 mVs^{-1} scan rate in 1 M Na_2SO_4 electrolyte. MnS_2 nanoparticles showed good rate capability feature with 297 Fg^{-1} capacitance retention at the higher scan rate of 100 mVs^{-1}. MnS_2//MoS_2 asymmetric supercapacitor achieved excellent specifications of 41.7 $Whkg^{-1}$ energy density and 450 Wkg^{-1} power density to power up 205 red light emitting diodes with high glow intensity.

Acknowledgement

Authors are thankful to Department of Science and Technology-Science and Engineering Research Board (DST-SERB), New Delhi India for their financial support through research project no. SERB/F/7448/2016-17 dated 13 January, 2017.

This study was supported by the National Research Foundation of Korea (NRF) grant funded by the Korea government (MSIT) (No.2017R1E1A1A01074550).

Appendix A. Supplementary data

Supplementary data to this article can be found online at https://doi.org/10.1016/j.electacta.2019.01.185.

References

[1] Y. Jin, C. Zhao, Q. Jiang, C. Ji, Mesoporous NiCoP microflowers as a superior electrode material for supercapacitors, Appl. Surf. Sci. 450 (2018) 170–179.
[2] H. Liang, C. Xia, A.H. Emwas, D.H. Anjum, X. Miao, H.N. Alshareef, Phosphine plasma activation of α-Fe_2O_3 for high energy asymmetric supercapacitors, Nano Energy 49 (2018) 155–162.
[3] Y. Wang, Y.Z. Zhang, D. Dubbink, J.E. Elshof, Inkjet printing of δ-MnO_2 nanosheets for flexible solid-state microsupercapacitor, Nano Energy 49 (2018) 481–488.
[4] N.G. Bretesche, O. Crosnier, C. Payen, F. Favier, T. Brousse, Nanocrystalline $FeWO_4$ as a pseudocapacitive electrode material for high volumetric energy density supercapacitors operated in an aqueous electrolyte, Electrochem. Commun. 57 (2015) 61–64.
[5] J. Eskusson, P. Rauwel, J. Nerut, A. Janes, A hybrid capacitor based on Fe_3O_4-graphene nanocomposite/few-layer graphene in different aqueous electrolytes, J. Electrochem. Soc. 163 (13) (2016) A2768–A2775.
[6] M. Wang, S. Cheng, G. Dang, F. Min, H. Li, Q. Zhang, J. Xie, Solvothermal synthesized γ-Fe_2O3/graphite composite for supercapacitor, Int J Electrochem Sci 12 (2017) 6292–6303.
[7] L. Shen, L. Du, S. Tan, Z. Zang, C. Zhao, W. Mai, Flexible electrochromic supercapacitor hybrid electrodes based on tungsten oxide films and silver nanowires, Chem. Commun. 52 (2016) 6296–6299.
[8] H. Cheng, Z.G. Lu, J.Q. Deng, C.Y. Chung, K. Zhang, Y.Y. Li, A facile method to improve the high rate capability of Co_3O_4 nanowire array electrodes, Nano Res 3 (2010) 895–901.
[9] W. Wei, L. Mi, Y. Gao, Z. Zheng, W. Chen, X. Guan, Partial ion-exchange of nickel-sulfide-derived electrodes for high performance supercapacitors, Chem. Mater. 26 (2014) 3418–3426.
[10] K.A. Owusu, L. Qu, J. Li, Z. Wang, K. Zhao, C. Yang, K.M. Hercule, C. Lin, C. Shi, Q. Wei, L. Zhou, L. Mai, Low-crystalline iron oxide hydroxide nanoparticle anode for high-performance supercapacitors, Nat. Commun. 8 (2017) 1–11.
[11] S. Sun, T. Zhai, C. Liang, S.V. Savilov, H. Xi, Boosted crystalline/amorphous $Fe_2O_{3-\delta}$ core/shell heterostructure for flexible solid-state pseudocapacitors in large scale, Nano Energy 45 (2018) 390–397.
[12] L. Shen, J. Wang, G. Xu, H. Li, H. Dou, X. Zhang, $NiCo_2S_4$ nanosheets grown on nitrogen-doped carbon foams as an advanced electrode for supercapacitors, Adv Energy Mater 5 (2015) 1–7.
[13] S. Peng, L. Li, H.B. Wu, S. Madhavi, X.W. Lou, Controlled growth of $NiMoO_4$ nanosheet and nanorod arrays on various conductive substrates as advanced electrodes for asymmetric supercapacitors, Adv Energy Mater 5 (2015) 1–7.
[14] M. Lee, S.K. Balasingam, H.Y. Jeong, W.G. Hong, H.B.R. Lee, B.H. Kim, Y. Jun, One-step hydrothermal synthesis of graphene decorated V_2O_5 nanobelts for enhanced electrochemical energy storage, Sci. Rep. 5 (2015) 1–8.
[15] D.P. Dubal, N.R. Chodankar, G.S. Gund, R. Holze, C.D. Lokhande, P.G. Romero, Asymmetric supercapacitors based on hybrid CuO@reduced graphene oxide@sponge versus reduced graphene oxide@sponge electrodes, Energy Technol. 3 (2015) 168–176.
[16] N. Kurra, N.A. Alhebshi, H.N. Alshareef, Microfabricated pseudocapacitors using $Ni(OH)_2$ electrodes exhibit remarkable volumetric capacitance and energy density, Adv Energy Mater 5 (2015) 1–9.
[17] B.L. Ellis, P. Knauth, T. Djenizian, Three-dimensional self-supported metal oxides for advanced energy storage, Adv. Mater. 26 (2014) 3368–3397.
[18] W. Chen, C. Xi, H.N. Alshareef, One-step electrodeposited nickel cobalt sulfide nanosheet arrays for high-performance asymmetric supercapacitors, ACS Nano 8 (2014) 9531–9541.
[19] S. Shahrokhian, R. Mohammadi, M.K. Aminic, In situ electrochemical exfoliation of highly oriented pyrolytic graphite as a new substrate for electrodeposition of flower like nickel hydroxide: application as a new high-performance supercapacitor, Electrochim. Acta 206 (2016) 317–327.
[20] R. Yuksel, S. Coskun, Y.E. Kalay, H.E. Unalan, Flexible, silver nanowire network nickel hydroxide core-shell electrodes for supercapacitors, J. Power Sources 328 (2016) 167–173.
[21] Z. Yu, L. Tetard, L. Zhai, J. Thomas, Supercapacitor electrode materials: nanostructures from 0 to 3 dimensions, Energy Environ. Sci. 8 (2015) 702–730.
[22] S. Liu, S.C. Lee, U.M. Patil, C. Ray, K.V. Sankar, K. Zhang, A. Kundu, S. kang, J.H. Park, S.C. Jun, Controllable sulfuration engineered NiO nanosheets with enhanced capacitance for high rate supercapacitors, J. Mater. Chem. 5 (2017) 4543–4549.
[23] S.L. Zhang, L. Zhou, H.B. Wu, R. Xu, X.W. Lou, Unusual formation of single-crystal manganese sulfide microboxes co-mediated by the cubic crystal structure, Angew. Chem. Int. Ed. 51 (2012) 7267–7270.
[24] Z. Chen, Z. Wan, T. Yang, M. Zhao, X. Lv, H. Wang, X. Ren, X. Mei, Preparation of nickel cobalt sulfide hollow nanocolloids with enhanced electrochemical property for supercapacitors application, Sci. Rep. 6 (2016) 1–8.
[25] B. You, Y. Sun, Hierarchically porous nickel sulfide multifunctional superstructures, Adv Energy Mater 6 (2016) 1–7.
[26] D.R. Cummins, H.B. Russell, J.B. Jasinski, M. Menon, M.K. Sunkara, Iron sulfide (FeS) nanotubes using sulfurization of hematite nanowires, Nano Lett. 13 (2013) 2423–2430.
[27] H. Liu, F.X. Ma, C.Y. Xu, L. Yang, Y. Du, P.P. Wang, S. Yang, L. Zhen, Sulfurizing-induced hollowing of Co_9S_8 microplates with nanosheet units for highly efficient water oxidation, ACS Appl. Mater. Interfaces 9 (2017) 11634–11641.
[28] H. Chen, J. Jiang, L. Zhang, H. Wan, T. Qi, D. Xia, Highly conductive $NiCo_2S_4$ urchin-like nanostructures for high-rate pseudocapacitors, Nanoscale 5 (2013) 8879–8883.
[29] S. Liu, K.V. Sankar, A. Kundu, M. Ma, J.Y. Kwon, S.C. Jun, Honeycomb-like interconnected network of nickel phosphide hetero-nanoparticles with superior electrochemical performance for supercapacitors, ACS Appl. Mater. Interfaces 9 (2017) 21829–21838.
[30] H. Zhang, D.H. Ha, R. Hovden, L.F. Kourkoutis, R.D. Robinson, Controlled synthesis of uniform cobalt phosphide hyperbranched nanocrystals using tri-n-octylphosphine oxide as a phosphorus source, Nano Lett. 11 (2011) 188–197.
[31] M.N. Siddiqui, Z.H. Yamani, B. Merzougui, M. Qamar, A. Adam, M.H. Suliman, Interconnected hollow cobalt phosphide grown on carbon nanotubes for hydrogen evolution reaction, ACS Appl. Mater. Interfaces 10 (2018) 29407–29416.
[32] L. Zhang, H.B. Wu, Y. Yan, X. Wang, X.W. Lou, Hierarchical MoS_2 microboxes constructed by nanosheets with enhanced electrochemical properties for lithium storage and water splitting, Energy Environ. Sci. 7 (2014) 3302–3306.
[33] L. Liu, Z. Yang, H. Liang, H. Yang, Y. Yang, Facile synthesis of $MnCO_3$ hollow dumbbells and their conversion to manganese oxide, Mater. Lett. 64 (2010) 2060–2063.
[34] B.J. Fei, Y. Cui, X. Yan, W. Qi, Y. Yang, K. Wang, Q. He, J. Li, Controlled preparation of MnO_2 hierarchical hollow nanostructures and their application in water treatment, Adv. Mater. 20 (2008) 452–456.
[35] P. Pal, S.K. Pahari, A.K. Giri, S. Pal, H.C. Bajaj, A.B. Panda, Hierarchically order porous lotus shaped nano-structured MnO_2 through $MnCO_3$: chelate mediated growth and shape dependent improved catalytic activity, J. Mater. Chem. 1 (2013) 10251–10258.
[36] X. Cao, H. Li, J. He, L. Kang, R. Jiang, F. Shi, H. Xu, Z. Lei, Z.H. Liu, Preparation and formation process of α-MnS@MoS_2 microcubes with hierarchical core/shell structure, J. Colloid Interface Sci. 507 (2017) 18–26.
[37] Y. Xin, L.Y. Cao, J.F. Huang, J. Liu, J. Fei, C.Y. Yao, Influence of S/Mn molar ratio on the morphology and optical property of γ-MnS thin films prepared by microwave hydrothermal, J Alloys Compd 549 (2013) 1–5.
[38] R.B. Pujari, A.C. Lokhande, A.A. Yadav, J.H. Kim, C.D. Lokhande, Synthesis of

MnS microfibers for high performance flexible supercapacitors, Mater. Des. 108 (2016) 510–517.
[39] M.S. Javed, X. Han, C. Hu, M. Zhou, Z. Huang, X. Tang, X. Gu, Tracking pseudocapacitive contribution to superior energy storage of MnS nanoparticles grown on carbon textile, ACS Appl. Mater. Interfaces 8 (2016) 24621–24628.
[40] Y. Tang, T. Chen, S. Yu, Morphology controlled synthesis of monodispersed manganese sulfide nanocrystals and their primary application in supercapacitors with high performances, Chem. Commun. 51 (2015) 9018–9021.
[41] Y. Tang, T. Chen, S. Yu, Y. Qiao, S. Mu, J. Hu, F. Gao, Synthesis of graphene oxide anchored porous manganese sulfide nanocrystals via the nanoscale Kirkendall effect for supercapacitors, J. Mater. Chem. 3 (2015) 12913–12919.
[42] Z. Ma, G. Shao, Y. Fan, G. Wang, J. Song, D. Shen, Construction of hierarchical α-MnO_2 nanowires@ultrathin δ-MnO_2 nanosheets core-shell nanostructure with excellent cycling stability for high-power asymmetric supercapacitor electrodes, ACS Appl. Mater. Interfaces 8 (2016) 9050–9058.
[43] S. Zhu, L. Li, J. Liu, H. Wang, T. Wang, Y. Zhang, L. Zhang, R.S. Ruoff, F. Dong, Structural directed growth of ultrathin parallel birnessite on β-MnO_2 for high-performance asymmetric supercapacitors, ACS Nano 12 (2018) 1033–1042.
[44] H. Xu, X. Hu, H. Yang, Y. Sun, C. Hu, Y. Huang, Flexible asymmetric microsupercapacitors based on Bi_2O_3 and MnO_2 nanoflowers: larger areal mass promises higher energy density, Adv Energy Mater 5 (2015) 1401882.
[45] M. Cakici, K.R. Reddy, F.A. Marroquin, Advanced electrochemical energy storage supercapacitors based on the flexible carbon fiber fabric-coated with uniform coral-like MnO_2 structured electrodes, Chem. Eng. J. 309 (2017) 151–158.
[46] F. Barzegar, A. Bello, J.K. Dangbegnon, N. Manyala, X. Xia, Asymmetric supercapacitor based on activated expanded graphite and pinecone tree activated carbon with excellent stability, Appl. Energy 207 (2017) 417–426.
[47] X. Yang, L. Zhao, J. Lian, Arrays of hierarchical nickel sulfides/MoS_2 nanosheets supported on carbon nanotubes backbone as advanced anode materials for asymmetric supercapacitor, J. Power Sources 343 (2017) 373–382.
[48] S. Wena, Y. Liu, F. Zhu, R. Shao, W. Xu, Hierarchical MoS_2 nanowires/$NiCo_2O_4$ nanosheets supported on Ni foam for high-performance asymmetric supercapacitors, Appl. Surf. Sci. 428 (2018) 616–622.
[49] Y. Ouyang, X. Xia, H. Ye, L. Wang, X. Jiao, W. Lei, Q. Hao, Three-dimensional hierarchical structure ZnO@C@NiO on carbon cloth for asymmetric supercapacitor with enhanced cycle stability, ACS Appl. Mater. Interfaces 10 (2018) 3549–3561.
[50] P.R. Deshmukh, Y. Sohn, W.G. Shin, Electrochemical performance of facile developed aqueous asymmetric $(Fe,Cr)_2O_3$//MnO_2 supercapacitor, Electrochim. Acta 285 (2018) 381–392.
[51] Z. Qiu, D. He, Y. Wang, X. Zhao, W. Zhao, H. Wu, High performance asymmetric supercapacitors with ultrahigh energy density based on hierarchical carbon nanotubes@NiO core-shell nanosheets and defect-introduced graphene sheets with hole structure, RSC Adv. 7 (2017) 7843–7856.
[52] L. Halder, A. Maitra, A.K. Das, R. Bera, S.K. Karan, S. Paria, A. Bera, S.K. Si, B.B. Khatua, High performance advanced asymmetric supercapacitor based on ultrathin and mesoporous $MnCo_2O_{4.5}$-$NiCo_2O_4$ hybrid and iron oxide decorated reduced graphene oxide electrode materials, Electrochim. Acta 283 (2018) 438–447.